Understanding reversibility of lithium–oxygen batteries based on LiOH formation and decomposition

Xiahui Zhang,[1] Panpan Dong,[1] Seunghyo Noh,[2] Xianghui Zhang,[3] Younghwan Cha,[1] Su Ha,[3] Ji-Hoon Jang,[2] and Min-Kyu Song[1,*]

1 School of Mechanical and Materials Engineering, Washington State University, Pullman, WA 99164, USA.

2 Institute of Fundamental and Advanced Technology, R&D Division, Hyundai Motor Company, Uiwang 16082, Republic of Korea.

3 Voiland School of Chemical Engineering and Bioengineering, Washington State University, Pullman, WA 99164, USA.

* Materials & Correspondence

Prof. M. -K. Song

E-mail address: minkyu.song@wsu.edu

Abstract

Lithium–oxygen batteries based on four-electron conversion to LiOH have demonstrated great potential for next-generation high-energy batteries. However, the understanding of LiOH-based cathode chemistry remains incomplete. Here, we use systematic characterization techniques to study LiOH chemistry, revealing that "high-performance" LiOH chemistry is achieved at the expense of electrolyte degradation and is irreversible in commonly used liquid organic electrolytes. LiOH forms via four-electron reduction of O_2 during discharge, whereas LiOH decomposes via one-electron oxidation during charge. This one-electron oxidation of LiOH generates surface-reactive hydroxyl species that aggressively degrade organic electrolytes. The reaction mechanisms are further supported by computational studies. Our findings suggest that the key to enable reversible LiOH chemistry is bypassing surface-reactive hydroxyl formation or using stable solid-state electrolytes, which can be explored by future research. Our findings also shed lights on the reversibility of four-electron cathode chemistries in other metal–air batteries.

Main text

High-energy lithium–oxygen (Li–O_2) batteries have been considered as one of the most promising energy storage systems. However, commonly studied Li–O_2 batteries based on Li_2O_2 as discharge product still face critical challenges such as low energy efficiency, poor rate performance, and short cycle life[1-4]. These challenges are mainly due to insulating and reactive nature of Li_2O_2, leading to slow kinetics and parasitic reactions. Alternatively, several other discharge products have also been reported[5-7], such as LiOH, LiO_2, and Li_2O. Among them, Li–O_2 batteries based on LiOH chemistry have shown great energy efficiency and cycling, rate performance at room temperature[5], and thus have attracted many attentions[8-13]. More importantly, Li–O_2 batteries will ultimately operate with an open system in air where moisture inevitably exists, i.e., Li–air batteries[8,9]. And LiOH chemistry can be operated in high humid environments[10], thus rendering it more practical than other oxygen cathode chemistries. Therefore, understanding LiOH chemistry is crucial for developing high-performance Li–O_2 batteries for practical applications.

During discharge, LiOH forms via four-electron conversion ($O_2 + 2H_2O + 4Li^+ + 4e^- \rightarrow 4LiOH$). Many studies have reported that efficient catalysts for O–O bond cleavage (e.g., MnO_2, Ru, and LiI) can lead to LiOH formation in the presence of water[5,11-15], whereas Li_2O_2 dominates as the discharge product without such catalysts[16-18]. Our previous work further demonstrated that, even though such catalysts are electrically isolated by a separator, LiOH still forms via a chemically catalytic process[19]. Despite these findings, the understanding of reaction pathways for LiOH formation remains limited. Furthermore, $LiFePO_4$ electrode has been widely used as an alternative to Li anode when studying the effect of water on battery performance[20,21], but it remains unclear whether $LiFePO_4$ reference electrode alters reaction chemistry in the presence of water,

3

considering that iron oxides are generally good catalysts for O–O bond cleavage. Therefore, further investigation is needed to understand LiOH formation.

During charge, the debate continues as to whether LiOH decomposition truly releases O_2 ($4LiOH \rightarrow O_2 + 2H_2O + 4Li^+ + 4e^-$), which is extremely crucial for determining reversibility of LiOH chemistry. Some reports claim that LiOH can decompose and release O_2,[5,12,19] whereas others oppose this statement[20,22,23]. Recently, Liu et al.[20] found that LiOH chemistry is irreversible in Li–O_2 batteries based on dimethyl sulfoxide (DMSO) electrolyte, which was attributed to the formation of hydroxyl free radicals ($LiOH \rightarrow Li^+ + e^- + OH\cdot$) that aggressively attack DMSO electrolyte. However, we calculate that the standard redox potential for OH· radical formation is extremely high: $E^0(OH\cdot/LiOH)$ = ~4.9 V vs. Li/Li$^+$ (**Table S2**). This calculation suggests that it is thermodynamically unfavorable to generate OH· radicals at low charging potential (<3.5 V vs. Li$^+$/Li) in common Li–O_2 batteries based on LiOH chemistry (**Supplementary Note 1** for more discussions). Therefore, further knowledge is urgently needed to understand charge mechanisms of LiOH chemistry, especially in tetraethylene glycol dimethyl ether (TEGDME), the most widely used electrolyte solvent in Li–O_2 batteries.

Herein, we aim to comprehensively understand formation and decomposition chemistry of LiOH and carefully examine its reversibility in Li–O_2 batteries. We prepared a ruthenium/carbon nanotube (Ru/CNT) as model cathode catalyst and a series of electrolytes with controlled water contents. To study discharge and, especially, charge processes of LiOH chemistry, we used systematic characterization tools, such as galvanostatic intermittent titration technique (GITT), isotope-labeled Raman spectroscopy, isotope-labeled mass spectrometry (MS), operando cell pressure measurement, and nuclear magnetic resonance (NMR). We found that LiOH chemistry enables a low initial charge plateau at ~3.4 V vs. Li$^+$/Li and good cyclability up to 150 cycles, and

even longer cycling performance at 294 cycles was achieved when the cut-off charge potential was controlled at 4.15 V vs. Li$^+$/Li. However, it is irreversible in conventional liquid organic electrolytes (e.g., TEGDME- or DMSO-based) at the expense of electrolyte degradation. We further propose that LiOH forms via four-electron reduction on Ru catalyst, whereas LiOH decomposes via one-electron oxidation to surface-reactive hydroxyl species (OH*, where * represents surface adsorption site) that aggressively degrades the electrolyte. The proposed reaction mechanisms are further supported by density-functional theory (DFT) calculations. We anticipate that our findings will pave the path for reversible, practical Li–O$_2$ batteries based on LiOH chemistry and provide insights to other metal–air batteries.

Results and Discussion

Characterization of Ru/CNT catalyst and wet electrolytes. Given that Ru-based materials have shown great activity towards oxygen evolution reaction (OER)[24], we synthesized Ru/CNT catalyst as cathode material. Small Ru nanoparticles (3–5 nm) are well dispersed on CNT substrates, as revealed by transmission electron microscopy (TEM), Energy-dispersive X-ray spectroscopy (EDS), and X-ray diffraction (XRD) results (**Figs. 1a,b** and **S3**). Besides, Ru nanoparticles have a native oxide layer on the surface (~27 at% RuO$_2$) as revealed by X-ray photoelectron spectroscopy (XPS) (**Figs. 1c** and **S4a–c**), owing to high affinity of Ru for oxygen[25,26].

Water is used as proton source for LiOH formation. We therefore prepared a series of H$_2$O/TEGDME mixtures with 0–20 wt% H$_2$O, and a mixture of x wt% H$_2$O and (100−x) wt% TEGDME is denoted as "x%-H$_2$O/TEGDME". Besides as proton source, water may affect solvating power of water-added electrolytes. It is established that discharge–charge mechanisms and related kinetics largely depend on the solvating power of the electrolyte[16,27], which is

characterized by Guttman acceptor number (AN) and donor number (DN). A high-DN or high-AN electrolyte has relatively high solubility of discharge intermediates, and thus induces a solution-mediated growth mechanism and better kinetics[16,28]. Thus, solvating power of wet electrolytes should be studied to understand discharge–charge mechanisms. Here, we determined the DN of wet electrolyte solvents by ^{23}Na NMR measurements (**Supplementary Note 2** for details). **Figure. 1d,e** reveals the almost linear plot of ^{23}Na chemical shift vs. DN of known solvents, which can be used to determine the DN of unknown solvents. The DN of anhydrous TEGDME increases from 16.6 to 25.0 kcal mol^{-1} after adding 20 wt% H_2O (**Fig. 1e** and **Table S4**). We therefore anticipate that wet electrolytes will induce solution-mediated growth mechanism and deliver better kinetics.

Aqueous electrolytes typically have shown narrow electrochemical stability window, and thus electrochemical stability of wet electrolytes is evaluated by linear sweep voltammetry (LSV). LSV results reveal that the electrochemical stability window narrows from 0.82–5.1 to 1.88–4.75 V vs. Li$^+$/Li with increasing water content from 0 to 20 wt% (**Figs. 1f**, **S9**, and **S10**). **Figure 1f** presents the anodic LSV curves of TEGDME-based electrolytes, revealing the decreased oxidative stability with increased water content. In other words, adding water improves solvating power of a low-DN solvent but compromises its electrochemical stability window.

Electrochemical performance of LiOH chemistry with Ru/CNT cathode and LiFePO$_4$ reference. In this study, Li–O$_2$ coin cells were assembled with an oxygen cathode, a glass fiber separator soaked with 1 M bis(trifluoromethane)sulfonimide lithium salt (LiTFSI) in x%-H$_2$O/TEGDME electrolyte, and a LiFePO$_4$ reference electrode. Here, LiFePO$_4$ reference electrode was used as alternative to Li anode that will severely corrode in wet environments. As discussed in detail in **Supplementary Note 4**, the extreme care should be taken when selecting reference

6

electrode for studying the effect of water in Li–O_2 batteries, because common reference/counter electrodes (e.g., Pt, Ag/Ag^+, and $LiFePO_4$) are good catalysts for H_2O_2 decomposition (O–O cleavage) and thus lead to LiOH formation. Nonetheless, $LiFePO_4$ electrode still can be used as reference electrode for studying LiOH chemistry, especially for charge mechanism.

Electrochemical performance of LiOH chemistry is evaluated by galvanostatic discharge–charge test. **Figure 2a** shows voltage profiles of Ru/CNT in wet electrolytes. In 20%-H_2O/TEGDME electrolyte, the Ru/CNT cathode revealed the lowest voltage gap between discharge and charge at 0.62 V. Surprisingly, we observed that the nominal charge overpotential for LiOH oxidation into O_2 is negative at the beginning of charge process (**Fig. S16d**), suggesting a different charge mechanism other than OER for LiOH chemistry ($E^0 = 3.32$ V vs. Li/Li^+; **Table S2**). Besides, additional charge plateaus at >3.8V were observed. Li et al.[12] also observed this feature when LiOH is discharge product, which was attributed to the increased resistance owing to gas bubbles. However, we reveal that this multiple-stage charge behavior is actually associated with complex side reactions and will be discussed later (**Fig. 5**). As shown in **Fig. S16b**, the Ru/CNT cathode exhibited 0.4 V lower charge potential than CNT in 20%-H_2O/TEGDME electrolyte, indicating high catalytic activity of Ru catalyst toward LiOH oxidation, owing to the appropriate binding energy toward oxygen species as demonstrated in water splitting[29]. Subsequently, we studied the side products on the cathode and in the electrolyte after the first cycle by *ex situ* NMR measurements (**Fig. S17**). The Ru/CNT cathode showed no obvious accumulation of insulating side products (lithium acetate, CH_3CO_2Li; lithium formate, HCO_2Li) on the cathode after charge. In contrast, the bare CNT cathode accumulated large amounts of CH_3CO_2Li and HCO_2Li. This comparison reveals that the Ru catalyst could promote the decomposition of LiOH

7

during charge and suppresses the accumulation of insulating side products on the cathode, leading to less cathode passivation.

Figure 2b,c shows cycling performance of the Ru/CNT cathode in 0%- and 20%-H_2O/TEGDME electrolyte, respectively. In 0%-H_2O/TEGDME electrolyte, the Ru/CNT cathode showed a large initial voltage gap of 1.1 V at the middle of discharge and charge, with a poor cycle life of 26 cycles. In 20%-H_2O/TEGDME electrolyte, however, the Ru/CNT cathode exhibited a much lower initial voltage gap of 0.6 V and much longer cycle life up to 150 cycles without capacity fading. Interestingly, a new obvious discharge plateau at ~3 V appeared at the 5th cycle in 0%- and 20%-H_2O/TEGDME electrolytes (**Fig. S22**). This feature can also be found in other works[17, 30-33], but unfortunately it is not fully understood. As discussed in detail in **Supplementary Note 7**, we attribute this additional discharge plateau to proton-coupled four-electron reduction of O_2 to water ($O_2 + 4H^+ + 4e^- \rightarrow 2H_2O$). In this reaction, proton is from acidic products like formic acid in cycled electrolytes as revealed by NMR measurements (**Fig. S17b**) and pH analysis (**Fig. S24**), which is discussed in detail in **Supplementary Note 8**. The formation mechanism of acidic products will be discussed later (**Fig. 5**).

The Ru/CNT cathode also showed a low initial voltage gap of 0.8 V at high current densities of 250 and 500 mA g^{-1} (**Fig. 2d**), with a long cycle life of 91 and 44 cycles (**Fig. S21**), respectively, demonstrating good rate performance. **Figure 2e** shows the summary of cycling and rate performance of Ru/CNT cathode in 0%- and 20%-H_2O/TEGDME electrolytes.

Thus far, we have demonstrated "high-performance" LiOH chemistry using Ru/CNT cathode in 20%-H_2O/TEGDME electrolyte, which can be ascribed to the high solvating power of 20%-H_2O/TEGDME electrolyte and high-efficiency Ru catalyst. In the following sections, we

explore reaction mechanisms of LiOH chemistry by systematic characterization techniques and theoretical analysis.

Four-electron discharge process of LiOH chemistry with Ru/CNT cathode. We performed XRD and XPS measurements (**Figs 3a–c**) to study the composition of discharged Ru/CNT cathodes in anhydrous (0% H_2O) and various wet electrolytes. The discharge product evolves from amorphous Li_2O_2 into Li_2O_2/LiOH mixture then finally into LiOH with increasing water content from 0 to 20%, indicating that water is indispensable for LiOH formation. When H_2O was replaced by D_2O, Raman spectra reveal that LiOD formed on the Ru/CNT cathode in 20%-D_2O/TEGDME electrolyte (**Fig. 3d**), further confirming water as the proton source of lithium hydroxide. The morphology of discharge products was also evolved from thin film in 0%-H_2O/TEGDME (**Fig. 3f**) to micro-sized nanosheets in 20%-H_2O/TEGDME (**Fig. 3g**), revealing that water can induce solution-driven growth by increasing solvating power of the electrolyte (**Fig. 1e**).

GITT measurements were performed to understand discharge mechanism. **Figure 4a,b** shows GITT results for the Ru/CNT cathode in 0%- and 20%-H_2O/TEGDME electrolyte, respectively. In 0%-H_2O/TEGDME electrolyte, the open-circuit potential (OCP) after relaxation remained at ~2.9 V over the course of discharge, corresponding to $O_2 + 2Li^+ + 2e^- \leftrightarrow Li_2O_2$ ($E^0 =$ 2.96 V vs. Li/Li^+, **Table S2**). Surprisingly, in 20%-H_2O/TEGDME electrolyte, the relaxed OCP remained at ~3.05 V, which is much lower than the standard potential of E^0(O_2/LiOH) at 3.32 V vs. Li/Li^+ (**Table S2**). We interpret this low relaxed OCP by mixed potential theory[34], which involves two redox couples (one with high redox potential and the other with low redox potential). At equilibrium (i.e., zero net current), the relaxed OCP falls between these two redox potentials (**Supplementary Note 9** for detailed discussion). Thus, GITT results suggest a new charge mechanism for LiOH oxidation, rather than four-electron OER.

9

To further understand the discharge mechanism, operando cell pressure measurements were performed. Theoretically, Li_2O_2 forms via 2 e^-/O_2 process, whereas LiOH forms via 4 e^-/O_2 process, revealing that LiOH chemistry consumes half amount of oxygen in Li_2O_2 chemistry for a given capacity. After cells were discharged to 0.25 mAh (**Figs. 4c,d**), the cell pressure dropped by ~11 mbar and ~20 mbar in 20%- and 0%-H_2O/TEGDME electrolyte, respectively, corresponding to LiOH and Li_2O_2 formation. Therefore, the drop of cell pressure for LiOH chemistry was roughly half of that for Li_2O_2 chemistry, suggesting a 4 e^-/O_2 process for LiOH formation.

Irreversible charge process of LiOH chemistry with Ru/CNT cathode. During charge, the GITT curves (**Fig. 4a**) shows that the relaxed OCP kept increasing in 0%-H_2O/TEGDME electrolyte, owing to the mixed potential caused by accumulation of insoluble side products on the cathode[35]. In contrast, the relaxed OCP remained almost same at the first charge plateau in 20%-H_2O/TEGDME electrolyte (**Fig. 4b**), suggesting a two-phase reaction. We hypothesize that this charge plateau is associated with one-electron oxidation of LiOH to generate surface-reactive OH* intermediates, which will be discussed in **Fig. 6**. And even if OH* intermediates attack TEGDME-based electrolyte, the majority of resultant side products should be soluble in the electrolyte (**Fig. S17b**) without passivating the cathode surface, leading to a low charge plateau and stable relaxed OCP. After the first charge plateau, the relaxed OCP kept increasing, which is attributed to the oxidation of side products from electrolyte degradation, followed by water oxidation at the last stage.

We further performed operando cell pressure measurements on charging to monitor gas evolution. The results reveal that Li_2O_2 chemistry shows gas evolution at the beginning of charge (**Fig. 4c**), corresponding to O_2 evolution and possibly CO_2 evolution from side reactions. However, LiOH chemistry shows even a slight pressure drop during the first charge plateau, followed by gas

evolution at the end of the first charge plateau (**Fig. 4d**). As discussed in detail in **Supplementary Note 10**, LiOH oxidation consumes O_2 at the first charge plateau owing to electrolyte degradation by hydroxyl intermediates, followed by CO_2 evolution from the oxidation of side products.

We further studied the composition of evolved gases on charging by *in situ* isotope-labeled MS. The results reveal that Li_2O_2 chemistry generates O_2 and CO_2 on charging (**Fig. S34**). In contrast, LiOH chemistry lacks O_2 and CO_2 evolution during the first half of charge process (**Figs. 4e**, **S36a–c**, and **S37a–c**). During the second half of charge process, only CO_2 evolution was observed, but still it lacks O_2 evolution (**Figs. 4f**, **S36d–f**, and **S37d–f**), indicating that the increased cell pressure for LiOH chemistry in **Fig. 4d** is associated with CO_2 evolution. We stress that 20% $H_2^{18}O$ was used for isotope-labeled MS measurements when studying LiOH chemistry, which eliminates false O_2 signals from the decomposition of amorphous Li_2O_2 or from potential air contamination.

Therefore, operando cell pressure measurements and *in situ* isotope-labeled MS spectra in this study have clearly demonstrated that LiOH chemistry is irreversible in conventional TEGDME-based organic electrolytes for lack of oxygen evolution on charging. These results are consistent with a few studies[20,23], but are contradictory to other studies[5,12,19]. For those studies that demonstrated O_2 evolution in LiOH chemistry, we infer that the discharge products might be mixtures of crystalline LiOH and amorphous Li_2O_2 in the presence of only trace amounts of water (e.g., a few hundreds of ppm), and thus O_2 evolution detected by MS might be actually from the decomposition of amorphous Li_2O_2, rather than LiOH.

To further elucidate charge mechanism of LiOH, we examined the cathodes at different states of charge (SoC), as shown in **Fig. 5a**, using *ex situ* SEM, XRD, FTIR, and NMR techniques. At 30% SoC, LiOH was partially removed as revealed by SEM and XRD (**Fig. 5b,d**), confirming

that the first charge plateau is associated with LiOH decomposition. Surprisingly, LiOH fully disappeared at only 70% SoC (i.e., the end of first charge plateau; **Fig. 5b,e**), suggesting non-Faraday's reactions participated in the first charge plateau (i.e., part of LiOH chemically reacts with acidic byproducts from electrolyte degradation). As mentioned before, electrolyte degradation by OH* generated acidic products (**Fig. S23**), which would react with LiOH via acid-base reaction, leading to early LiOH removal and thus multi-stage charge behaviors. FTIR and NMR results in **Fig. 5g,h** reveal that insoluble side products were deposited on the cathode at 70% SoC, including Li_2CO_3, HCO_2Li, and CH_3CO_2Li. Considering that TEGDME, $CH_3O(CH_2CH_2O)_4CH_3$, contains no ethyl groups ($-CH_2CH_3$), we infer that CH_3CO_2Li was most likely generated by a series of free-radical chain reactions[36], leading to chain growth from methyl to ethyl (**Supplementary Note 16** for details). At 100% SoC, the insoluble side products on the cathode were fully removed as revealed by FTIR and NMR. Nonetheless, many side products are soluble in degraded electrolytes, such as aldehydes and carboxylic acids, which were observed by NMR even at 100% SoC (**Figs. S17b** and **S38**). Combining MS, FTIR, and NMR results, we infer that CO_2 evolution at the second half of charge process is associated with decomposition of side products.

Besides TEGDME-based electrolytes, we also studied DMSO-based electrolytes for comparison. Similar results were also observed in 20%-H_2O/DMSO electrolyte (**Figs. S39–S42**). However, it showed the earlier LiOH removal at 50% SoC and lower charge potential than TEGDME-based electrolyte, which can be ascribed to the higher reactivity of DMSO toward OH intermediates causing "Nernstian shift".

To further demonstrate how electrolyte degradation affects cycling performance, we compared cycling performance of Ru/CNT cathode with different amounts of 20%-

12

H_2O/TEGDME electrolyte and with different cut-off charge potentials. When half of the electrolyte was used, the cycling performance was shortened by more than half from 150 down to 60 cycles (**Fig. S45**), mostly likely owing to the early depletion of the electrolyte due to degradation over cycling. We therefore suggest future studies should specify the amount of the electrolyte used. Considering that LiOH was fully removed at ~70% SoC in 20%-H_2O/TEGDME electrolyte, we performed cycling test with three controlled cut-off potentials (**Fig. S46**). At a low cut-off potential of 3.85 V, the cell only achieved 38 cycles, owing to the insufficient removal of insoluble side products on the cathode at low potential. On the other hand, the cell with a high cut-off potential of 4.85 V achieved 174 cycles, owing to the severe degradation of electrolytes at high potential. Interestingly, the cell with a middle cut-off potential of 4.15 V achieved the best cycling performance over 294 cycles, owing to the mitigation of both cathode passivation and electrolyte degradation.

Thus far, we have demonstrated that LiOH oxidation is irreversible in TEGDME-based electrolytes for lack of O_2 evolution, owing to the formation of surface-reactive OH* species that degrades organic electrolytes. Therefore, if organic components can be eliminated from electrolytes, Li–O_2 batteries based on LiOH should be reversible, such as aqueous or solid-state Li–O_2 batteries.

Reaction mechanism of LiOH chemistry and theoretical analysis by DFT calculations. From above experimental results, we proposed reaction mechanisms for LiOH chemistry in Ru-catalyzed cells with conventional liquid organic electrolytes in the presence of water, which are further investigated using DFT calculations. To guide the design of structural models for DFT calculations, we performed XPS measurements for Ru/CNT cathode at pristine (**Fig. 6a**),

13

discharged (**Fig. 6a**), and charged state (**Fig. 6c**), respectively. At pristine state, the Ru surface of Ru/CNT cathode is only slightly oxidized with 25% of RuO_2 (**Fig. 6a**), and thus one monolayer (1 ML) coverage of oxygen on Ru($10\bar{1}0$) plane was used as structural model for initial discharge process. On the other hand, Ru surface is largely oxidized at full discharge with 59% RuO_2 (**Fig. 6b**), especially at full recharge with 82% of RuO_2 (**Fig. 6c**), and thus RuO_2(001) plane was selected as structural model for charge process.

Figure 6d,e shows reaction pathways and corresponding energy diagrams using DFT calculations for LiOH formation. During discharge, O_2 is first electrochemically reduced to LiO_2^* via one-electron reduction, followed by chemical disproportionation of LiO_2^* to $Li_2O_2^*$. In the final step, the hydrolysis of $Li_2O_2^*$ leads to LiOH and regenerate active site. Overall, it is a net 4 e^- transfer reaction for LiOH formation. In general, 4 e^- transfer reactions involve scaling relations between adsorption energy of intermediates, leading to a minimum overpotential of 0.2–0.4 V, as suggested by theoretical studies[37]. Indeed, our calculation results show an overpotential of η_{DC} = 0.48 V (**Fig. 6e**), corresponding to the first electrochemical reduction as the rate-determining step. The subsequent chemical steps are down-hill in energy diagram (**Fig. 6e**).

Figure 6f,g shows reaction pathways and corresponding energy diagrams using DFT calculations for LiOH decomposition. During charge, LiOH is first electrochemically oxidized to *OH via one-electron oxidation, followed by H-atom abstraction from TEGDME by OH* and associated electrolyte degradation (**Supplementary Note 16** for details). Overall, it is a net 1 e^- transfer reaction for LiOH decomposition. This 1 e^- transfer reaction does not involve scaling relations, leading to a low onset charge potential of U_C =3.06 V vs. Li^+/Li, corresponding to a small overpotential of η_C = 0.26 V (**Fig. 6e**).

To further study the missing O_2 on charge, we calculated energy diagrams for 4 e$^-$ OER in LiOH chemistry (**Fig. S51**). Because of high energy barrier for O–O bond re-formation in typical Ru-based catalyst[29], O_2 evolution occurs at a high onset potential of $U_{OER} = 3.99$ V vs. Li$^+$/Li on RuO$_2$(001) planes. Given $U_{OER} > U_C$, LiOH is therefore preferably oxidized to form OH* via 1 e$^-$ transfer, instead of 4 e$^-$ OER, leading to low charge potential but lack of O_2 evolution.

Conclusion

In summary, this work demonstrates that the LiOH chemistry is irreversible for lack of O_2 evolution in commonly used liquid organic electrolytes, and its "high performance" is achieved at the expense of electrolyte degradation and is largely dependent on the amount of the electrolyte. We propose that LiOH forms via four-electron conversion of O_2 but decomposes via one-electron oxidation to surface-reactive OH* species that attacks electrolytes, which are further supported by DFT calculations. Given that LiOH chemistry can be operated in highly humid environments, we still believe it is very promising for practical Li–air batteries. As such, more fundamental research is needed to achieve reversible 4 e$^-$ LiOH chemistry. Therefore, we encourage the following research directions: (1) finding alternative reaction pathways for oxidizing 4 e$^-$ discharge products, such as using redox mediators; (2) using stable solid-state electrolytes or molten-salt electrolytes against surface-reactive OH* species.

Methods

Materials. TEGDME (99%), DME (99.5%), DMSO (99.9%), HMPA (99%), PC (99.7%), EC (99%), C$_6$H$_6$ (99.9%) were purchased from Sigma-Aldrich. All above solvents were stored over freshly activated 4A molecular sieves (Alfa Aesar). LiTFSI (99.95%) and LiClO$_4$ (99.99%), D$_2$O

(99.9 at% D), DMSO-d6 (99.9 at% D), deuterium chloride (35 wt% DCl in D_2O, 99 at% D), water-^{18}O (H_2O^{18}, 97 at% ^{18}O), polytetrafluoroethylene preparation (60 wt% PTFE in H_2O), 2-propanol (IPA, 99.9%), KO_2 powder, Li_2CO_3 (99%), and NaCl (99.5%) were purchased from Sigma-Aldrich. Ultrapure H_2O (Nanopure Analytical, 18.2 MΩ-cm) was used. LiTFSI and $LiClO_4$ were dried under vacuum at 120 °C overnight. High-purity O_2 (≥99.5%) was purchased from AL Compressed Gases. Multi-walled carbon nanotubes with –COOH functionalized (CNT, ≥95%, OD 20‒30 nm), Ketjenblack EC600JD carbon black (KB-600), and carbon nanofibers (CNF, PR-24-XT-HHT) were purchased from Nanostructured & Amorphous Materials, AkzoNobel, and Pyrograf Products, respectively.

Preparation of Electrodes and electrolytes. The preparation of Ru/CNT catalyst is described in **Supporting Information**. A typical oxygen cathode was fabricated by making a homogenized slurry of Ru/CNT catalyst or CNT (60 wt%), KB-600 (25 wt%), CNF (5 wt%), and PTFE (10 wt%) in IPA/H_2O mixture (1/4, v/v), followed by casting on a carbon paper (Spectracarb 2050A-0550, Fuel Cell Store). We note that ultrasonic homogenizer is effective to disperse hydrophobic carbon in IPA/H_2O mixture within a few seconds, achieving a good slurry. The electrodes and glass fiber membranes (GF/D, Whatman) were dried at 150 °C under vacuum overnight and then transferred into glove box without exposure to air. The areal loading of cathodes is calculated by total electrode materials excluding PTFE binder and is kept at 0.5±0.1 mg cm^{-2}. All $LiFePO_4$ reference electrodes (MTI Corporation, ~12 mg cm^{-2}) were partially pre-delithiated at ~20% prior to use, showing a stable average discharge–charge plateau at ~3.45 V vs. Li/Li^+. The electrolyte was prepared by dissolving 1 M LiTFSI in various solvents such as pure TEGDME or 20wt% H_2O in TEGDME. The water content in the anhydrous electrolyte was measured to be <5 ppm by a Karl Fisher coulometer (C20, Metter Toledo).

Cell assembly. All Li–O_2 cells in this study are CR2032-type coin cells (Wellcos Corporation) with 37×Φ1.4 mm open meshes, which are described previously[19]. Briefly, a typical coin cell was assembled by sandwiching a GF/D separator (Φ18 mm) between a LiFePO$_4$ reference (unless specified, Φ16 mm) and an oxygen cathode (Φ12 mm) in an Ar-filled glove box (MBraun, H_2O <0.5 ppm and O_2 <0.5 ppm). To better retract the cycled cathodes, we placed an extra Celgard 2400 separator (Φ18 mm) between the cathode and the GF/D separator. Unless specified, 200 µL of the electrolyte was used. After assembly, the cell was put into a 500-mL cell testing container and purged with high-purity O_2 for 10 min, followed by resting in O_2 for 6 hours prior to electrochemical testing. The humidity of the oxygen was measured to be <20 ppm by a humidity analyzer (EQ-RH-800-LD, MTI Corporation). We note that when cell testing for dry electrolyte (i.e., 0%-H_2O/TEGDME or 0%-H_2O/DMSO electrolyte), the cell container was filled with 10–20 g of activated 3A molecular sieves to remove any moisture in the cell testing setup.

***Ex-situ* analysis of cycled cathodes and electrolytes.** After retracted from the dissembled cells inside glovebox, all the cycled cathodes were washed with DME three times, followed by drying under vacuum for at least 1 hour, prior to any *ex-situ* analysis. When preparing XRD samples, Kapton tape was used to protect the cathodes from exposure to air. For Raman samples, the cathodes were placed between two quartz slides with the edge sealed by Kapton tape. For NMR samples, D_2O and DME (unless specified) were used to extract side products on cathodes and in electrolytes, respectively. We note that all cell parts were rinsed with DME three times to extract the electrolyte as much as possible. To improve the signal/noise ratio, the extracted electrolyte in DME was dried at room temperature under vacuum to remove DME, yielding the concentrated electrolyte. For quantitative ^{1}H NMR analysis, 10 µL of 2.5 wt% C_6H_6 in DMSO-d6 (~11.8 mg in total) was added as internal standards.

Theoretical calculations. Vienna Ab-initio Simulation Package (VASP) was utilized to calculate the total energies of model systems.[38] Projector Augmented Wave (PAW) pseudopotential replace the interaction potentials of the core electrons.[39] Exchange-correlation energy of electrons was calculated with the spin-polarized generalized gradient approximation (GGA) as implemented in the VASP software.[40] Kohn–Sham orbitals were expanded by plane waves up to a cut-off energy of 520 eV. Calculations were continued until the energy for ionic relaxation step was converged within 1×10^{-3} eV, and the criteria of electronic convergence for ground state energy is 1×10^{-4} eV. k-point of all the slab models is $3 \times 3 \times 1$. Based on experimental XPS analysis, discharge and charge processes were considered as O ML/Ru(0001) and RuO_2(001) slab model, respectively. Discharge process assumes the following three steps: (1.1) $* + Li^+ + e^- + O_2(g) \rightarrow LiO_2*$; (1.2) $LiO_2* \rightarrow \frac{1}{2}Li_2O_2* + \frac{1}{2}O_2(g)$; (1.3) $\frac{1}{2}Li_2O_2* + H_2O(l) + \frac{1}{2}O_2(g) \rightarrow LiOH* + \frac{3}{4}O_2(g)$. Charge process assumes the following two steps: (2.1) $LiOH* \rightarrow OH* + Li^+ + e^-$; (2.2) $OH* + TEGDME \rightarrow * + H_2O(l) + $ H-abstracted $TEGDME\cdot$. The change in Gibbs free energy (ΔG) for each step was calculated by the following equation: $\Delta G = \Delta E - T\Delta S + \Delta ZPE + neU$,[41] where ΔE, ΔS, and ΔZPE are the change of binding energy/enthalpy, entropy, and zero-point energy, respectively; *T, n, e, U* are temperature, number of electrons gained (i.e., positive for discharge and negative for charge), elementary charge, applied potential, respectively. The *neU* term was included to account for the energy shift of electrons by an applied potential *U* vs. Li^+/Li. We note that ΔG was referenced to the reactants, i.e., $\Delta G = 0$ at initial state in energy diagram. The equilibrium potential for a given reaction was calculated by $U_0 = -\Delta G^0/ne$, where ΔG^0 is the free energy change of the total reaction at U = 0.

Data availability

The data that support the findings of this study are available from the corresponding author upon reasonable request.

Acknowledgements

Author contributions

Xiahui Z. and M.-K. S. conceived the concept and designed the experiments. Xiahui Z., P. D., Xianghui Z., and Y.C. performed the experiments; S.N. performed DFT calculations; all authors contributed to the interpretation of data; Xiahui Z. wrote the manuscript, and all authors edited the manuscript; S.H., J. J., and M.-K.S. supervised this work. M.-K.S. led the multi-lab collaborations for this work.

Competing interests

The authors declare no conflict of interest.

Additional information

Supplementary Information is available for this paper.

References

1   Bruce, P. G., Freunberger, S. A., Hardwick, L. J. & Tarascon, J. M. Li–O_2 and Li–S batteries with high energy storage. *Nat. Mater.* **11**, 19-29, doi:10.1038/nmat3191 (2012).

2   Aurbach, D., McCloskey, B. D., Nazar, L. F. & Bruce, P. G. Advances in understanding mechanisms underpinning lithium–air batteries. *Nat. Energy* **1**, 16128 (2016).

3   Kwak, W.-J. *et al.* Lithium–Oxygen Batteries and Related Systems: Potential, Status, and Future. *Chem. Rev.* (2020).

4   Liu, T. *et al.* Current challenges and routes forward for nonaqueous lithium–air batteries. *Chem. Rev.* (2020).

5   Liu, T. *et al.* Cycling Li-O_2 batteries via LiOH formation and decomposition. *Science* **350**, 530-533 (2015).

6   Lu, J. *et al.* A lithium–oxygen battery based on lithium superoxide. *Nature* **529**, 377-382 (2016).

7   Xia, C., Kwok, C. & Nazar, L. A high-energy-density lithium-oxygen battery based on a reversible four-electron conversion to lithium oxide. *Science* **361**, 777-781 (2018).

8   Geng, D. *et al.* From lithium-oxygen to lithium-air batteries: challenges and opportunities. *Adv. Energy Mater.* **6**, 1502164 (2016).

9   Liu, L. *et al.* Critical Advances in Ambient Air Operation of Nonaqueous Rechargeable Li–Air Batteries. *Small*, 1903854 (2019).

10   Temprano, I. *et al.* Toward Reversible and Moisture-Tolerant Aprotic Lithium-Air Batteries. *Joule* **4**, 2501-2520 (2020).

11   Black, R. *et al.* Screening for superoxide reactivity in Li-O_2 batteries: effect on Li_2O_2/LiOH crystallization. *J. Am. Chem. Soc.* **134**, 2902-2905 (2012).

12   Li, F. *et al.* The water catalysis at oxygen cathodes of lithium–oxygen cells. *Nat. Commun.* **6**, 7843 (2015).

13   Tułodziecki, M. *et al.* The role of iodide in the formation of lithium hydroxide in lithium–oxygen batteries. *Energy Environ. Sci.* **10**, 1828-1842 (2017).

14   Liu, T. *et al.* Understanding LiOH Formation in a Li-O_2 battery with LiI and H_2O additives. *ACS Catal.* **9**, 66-77 (2018).

15   Lu, J. *et al.* Co_3O_4-Catalyzed LiOH Chemistry in Li–O_2 Batteries. *ACS Energy Lett.* **5**, 3681-3691 (2020).

16   Aetukuri, N. B. *et al.* Solvating additives drive solution-mediated electrochemistry and enhance toroid growth in non-aqueous Li–O_2 batteries. *Nat. Chem.* **7**, 50 (2015).

17   Schwenke, K. U., Metzger, M., Restle, T., Piana, M. & Gasteiger, H. A. The influence of water and protons on Li_2O_2 crystal growth in aprotic Li-O_2 cells. *J. Electrochem. Soc.* **162**, A573-A584 (2015).

18   Qiao, Y. *et al.* From O_2^- to HO_2^-: Reducing By-Products and Overpotential in Li-O_2 Batteries by Water Addition. *Angew. Chem. Int. Ed.* **56**, 4960-4964 (2017).

19   Zhang, X. *et al.* Enhanced Cycling Performance of Rechargeable Li–O_2 Batteries via LiOH Formation and Decomposition Using High-Performance MOF-74@CNTs Hybrid Catalysts. *Energy Storage Mater.* **17**, 167-177 (2019).

20   Liu, T. *et al.* Understanding LiOH Chemistry in a Ruthenium-Catalyzed Li-O_2 Battery. *Angew. Chem.* **129**, 16273-16278 (2017).

21   Mahne, N. *et al.* Singlet oxygen generation as a major cause for parasitic reactions during cycling of aprotic lithium–oxygen batteries. *Nat. Energy* **2**, 1-9 (2017).

22   Meini, S. *et al.* Rechargeability of Li–air cathodes pre-filled with discharge products using an ether-based electrolyte solution: implications for cycle-life of Li–air cells. *Phys. Chem. Chem. Phys.* **15**, 11478-11493 (2013).

23   Ma, S., Wang, J., Huang, J., Zhou, Z. & Peng, Z. Unveiling the complex effects of H_2O on discharge–recharge behaviors of aprotic lithium–O_2 batteries. *J. Phys. Chem. Lett.* **9**, 3333-3339 (2018).

24   Rossmeisl, J., Qu, Z.-W., Zhu, H., Kroes, G.-J. & Nørskov, J. K. Electrolysis of water on oxide surfaces. *J. Electroanal. Chem.* **607**, 83-89 (2007).

25   Nørskov, J. K. *et al.* Origin of the overpotential for oxygen reduction at a fuel-cell cathode. *J. Phys. Chem. B* **108**, 17886-17892 (2004).

26   Zhang, P.-F. *et al.* Synergetic Effect of Ru and NiO in the Electrocatalytic Decomposition of Li_2CO_3 to Enhance the Performance of a Li-CO_2/O_2 Battery. *ACS Catal.* **10**, 1640-1651 (2019).

27   Johnson, L. *et al.* The role of LiO_2 solubility in O_2 reduction in aprotic solvents and its consequences for Li-O_2 batteries. *Nat. Chem.* **6**, 1091-1099, doi:10.1038/nchem.2101 (2014).

28   Leverick, G. *et al.* Solvent-and Anion-Dependent Li^+–O_2^- Coupling Strength and Implications on the Thermodynamics and Kinetics of Li–O_2 Batteries. *J. Phys. Chem. C* **124**, 4953-4967 (2020).

29   Man, I. C. *et al.* Universality in oxygen evolution electrocatalysis on oxide surfaces. *ChemCatChem* **3**, 1159-1165 (2011).

30   Zhang, T. & Zhou, H. From Li–O_2 to Li–air batteries: carbon nanotubes/ionic liquid gels with a tricontinuous passage of electrons, ions, and oxygen. *Angew. Chem. Int. Ed.* **51**, 11062-11067 (2012).

31   Jung, H.-G., Hassoun, J., Park, J.-B., Sun, Y.-K. & Scrosati, B. An improved high-performance lithium–air battery. *Nat. Chem.* **4**, 579 (2012).

32   Asadi, M. *et al.* A lithium–oxygen battery with a long cycle life in an air-like atmosphere. *Nature* **555**, 502 (2018).

33   He, B. *et al.* Superassembly of Porous $Fe_{tet}(NiFe)_{oct}O$ Frameworks with Stable Octahedron and Multistage Structure for Superior Lithium–Oxygen Batteries. *Adv. Energy Mater.*, 1904262, doi:10.1002/aenm.201904262 (2020).

34   Revie, R. W. *Corrosion and corrosion control: an introduction to corrosion science and engineering*. 4th edn, (John Wiley & Sons, 2008).

35   McCloskey, B. D. *et al.* Twin problems of interfacial carbonate formation in nonaqueous Li–O_2 batteries. *J. Phys. Chem. Lett.* **3**, 997-1001 (2012).

36   Carey, F. A. & Sundberg, R. J. *Advanced organic chemistry: part A: structure and mechanisms*. 5th edn, (Springer Science & Business Media, 2007).

37   Seh, Z. W. *et al.* Combining theory and experiment in electrocatalysis: Insights into materials design. *Science* **355** (2017).

38   Kresse, G. & Furthmüller, J. Efficient iterative schemes for ab initio total-energy calculations using a plane-wave basis set. *Physical review B* **54**, 11169 (1996).

39   Blöchl, P. E. Projector augmented-wave method. *Physical review B* **50**, 17953 (1994).

40   Fiederling, R. *et al.* Injection and detection of a spin-polarized current in a light-emitting diode. *Nature* **402**, 787-790 (1999).

41   Rossmeisl, J., Nørskov, J. K., Taylor, C. D., Janik, M. J. & Neurock, M. Calculated phase diagrams for the electrochemical oxidation and reduction of water over Pt (111). *J. Phys. Chem. B* **110**, 21833-21839 (2006).

42   Naumkin, A. V., Kraut-Vass, A., Gaarenstroom, S. W. & Powell, C. J. Vol. NIST Standard Reference Database 20, Version 4.1   (National Institute of Standards and Technology (NIST), Gaithersburg MD, 2012).

43   Morgan, D. J. Resolving ruthenium: XPS studies of common ruthenium materials. *Surf. Interface Anal.* **47**, 1072-1079 (2015).
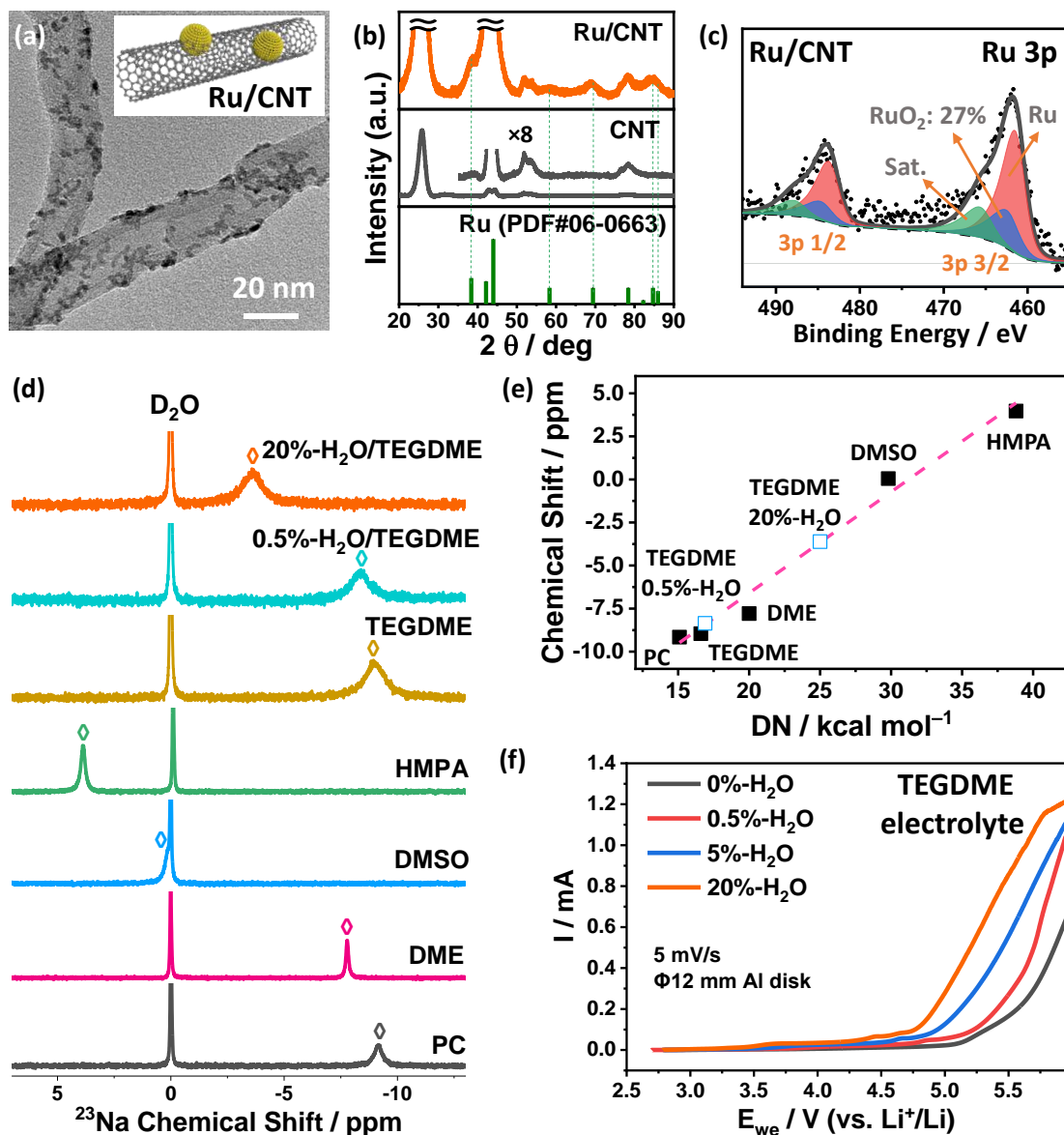
Figure 1 | Characterization of Ru/CNT catalyst and TEGDME-based electrolytes. (**a–c**) TEM, XRD, XPS results of the Ru/CNT catalyst, showing that Ru nanoparticles are uniformly dispersed on CNT and the surface of Ru nanoparticles is slightly oxidized (i.e., a native oxide layer). Inset in **a** schematically illustrates the Ru/CNT catalyst (color: CNT, gray; Ru, gold). The XPS Ru 3p in **c** shows spin-orbit splitting (i.e., Ru $3p_{1/2}$ and Ru $3p_{3/2}$ doublets), which can be further deconvoluted into three sets of doublets, corresponding to Ru, RuO_2, and satellite peaks[42,43] (**Table S3** for detailed peak assignments). (**d**) ^{23}Na NMR spectra of various electrolyte solvents. (**e**) The

linear relationships of ^{23}Na NMR chemical shift vs. donor number (DN) of various electrolyte solvents, showing that the DN of the TEGDME increases with the increase of water content. Note that: propylene carbonate (PC, 15.1 kcal mol^{-1}), 1,2-dimethoxyethane (DME, 18.6 kcal mol^{-1}), dimethyl sulfoxide (DMSO, 29.8 kcal mol^{-1}), hexamethylphosphoramide (HMPA, 38.8 kcal mol^{-1}), tetraethylene glycol dimethyl ether (TEGDME, 16.6 kcal mol^{-1}), 0.5%-H$_2$O/TEGDME (16.9 kcal mol^{-1}), 20%-H$_2$O/TEGDME (25.0 kcal mol^{-1}). (**f**) The anodic LSV curves of TEGDME-based electrolytes with various water contents, showing that their electrochemical stability decreases with the increase of water content. Note that 1 M bis(trifluoromethane)sulfonimide lithium salt (LiTFSI) was used.
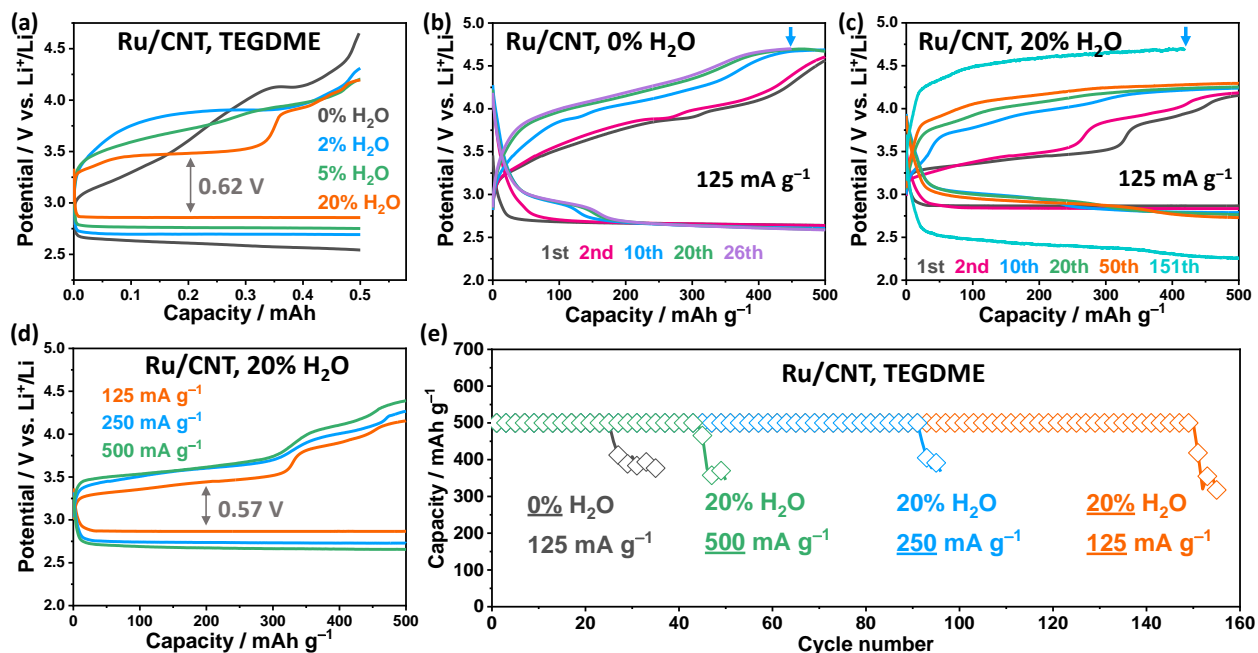

Figure 2 | Electrochemical performance of Ru/CNT cathode in TEGDME-based electrolyte. (**a**) Voltage profiles of Ru/CNT cathodes in TEGDME electrolytes with 0–20% H$_2$O added at a current of 50 µA. (**b–c**) Cycling performance of Ru/CNT cathodes in (**c**) 0%-H$_2$O/TEGDME electrolyte and (**d**) 20%-H$_2$O/TEGDME electrolyte at a current density of 125 mA g^{-1}, showing

that the Ru/CNT cathode exhibits much improved cycling performance in 20%-H_2O/TEGDME electrolyte when compared with that in dry electrolyte. Note that the blue arrows in **b** and **c** indicate the terminal of charge process at a cut-off potential of 4.65 V. (**d**) Rate performance of Ru/CNT cathodes in 20%-H_2O/TEGDME electrolyte at a current density of 125, 250, and 500 mA g^{-1}. (**e**) A summary of cycling and rate performance of Ru/CNT cathodes in 0%-H_2O/TEGDME electrolyte at a current density of 125 mA g^{-1} and 20%-H_2O/TEGDME electrolyte at a current density of 125, 250, and 500 mA g^{-1}.
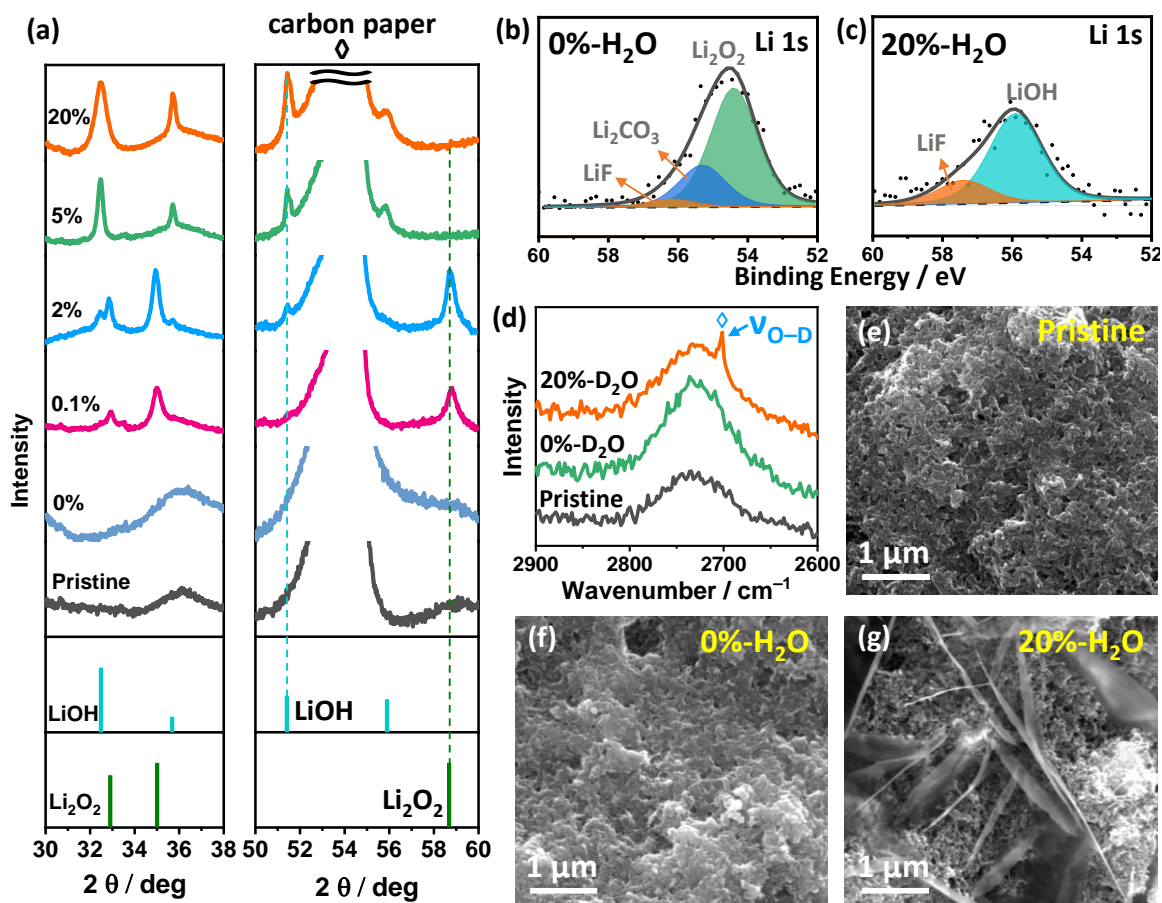

Figure 3 | The *ex-situ* characterization of discharge products in TEGDME-based electrolytes. (**a**) XRD patterns of pristine Ru/CNT cathode and discharged Ru/CNT cathodes in dry and various wet electrolytes (0.1wt%, 2wt%, 5wt%, and 20wt% H_2O in TEGDME), showing that the discharge

products evolve from amorphous Li_2O_2 to crystalline Li_2O_2, to mixture of Li_2O_2 and LiOH, finally to LiOH. (**b,c**) XPS Li 1s spectra of discharged Ru/CNT cathodes in (**b**) 0%-H_2O/TEGDME electrolyte and (**c**) 20%-H_2O/TEGDME electrolyte. (**d**) Raman spectra of pristine Ru/CNT cathode and discharged Ru/CNT cathodes in dry TEGDME and 20%-D_2O/TEGDME electrolytes, confirming that proton source in LiOH is from water. (**e–g**) SEM images of (**e**) the pristine Ru/CNT cathode and the discharged Ru/CNT cathodes in (**f**) dry and (**g**) 20wt% H_2O electrolytes, showing that amorphous Li_2O_2 forms in dry electrolyte and nanosheet-like LiOH form in 20%-H_2O/TEGDME electrolyte. Note that the cells were operated at a current of 50 µA and capacity of 0.5 mAh.
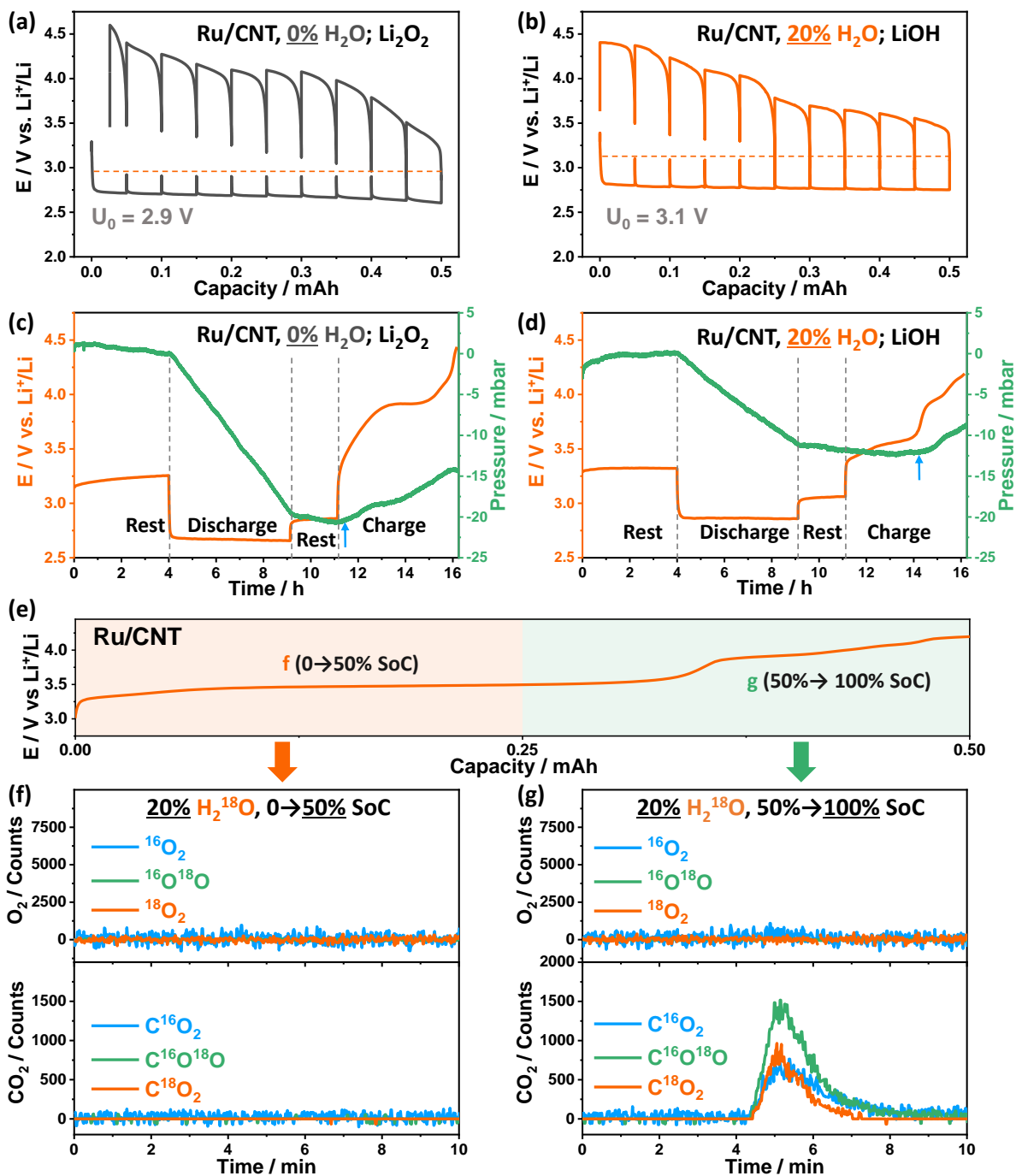
Figure 4 | Comparison of Li₂O₂ with LiOH chemistry by GITT, operando gas pressure measurements, and isotope-labeled MS. (**a–b**) GITT results of Ru/CNT cathodes in (**a**) 0%-H₂O/TEGDME electrolyte and (**b**) 20%-H₂O/TEGDME electrolyte at a capacity of 0.5 mAh, showing that two-phase reaction mechanism dominates ORR reactions in dry and wet electrolyte.

During charge, Ru/CNT cathode in dry electrolyte shows increasing OCP because of either the increasing ohmic drop or single-phase (i.e., solid-solution) reaction mechanism, whereas Ru/CNT cathode in wet electrolyte shows a charge plateau below 3.8 V because of two-phase reaction mechanism. (**c–d**) Operando pressure measurements of Ru/CNT cathodes in (**c**) 0%-H_2O/TEGDME electrolyte and (**d**) 20%-H_2O/TEGDME electrolyte at a capacity of 0.25 mAh. Note that blue arrows indicate the onset of pressure increase (i.e., gas evolution) during charging. The gas evolution starts right after the charge process in dry electrolyte, whereas the gas evolution happens at the second charge plateau of >3.8 V in 20%-H_2O/TEGDME electrolyte. (**e–f**) Isotope-labeled MS spectra of Ru/CNT cathodes in 20wt% $H_2^{18}O$ electrolyte and $^{16}O_2$ at (**e**) the first half of charge process of 0→0.25 mAh (i.e., 0→50% SoC) and (**f**) the second half of charge process of 0.25→0.5 mAh (i.e., 50%→100% SoC), showing that the charging process lacks O_2 evolution but generates CO_2 at the second charge plateau, including $C^{16}O_2$, $C^{16}O^{18}O$, $C^{18}O_2$. Note that "SoC" refers to state of charge and the cells were operated at a current of 50 µA.
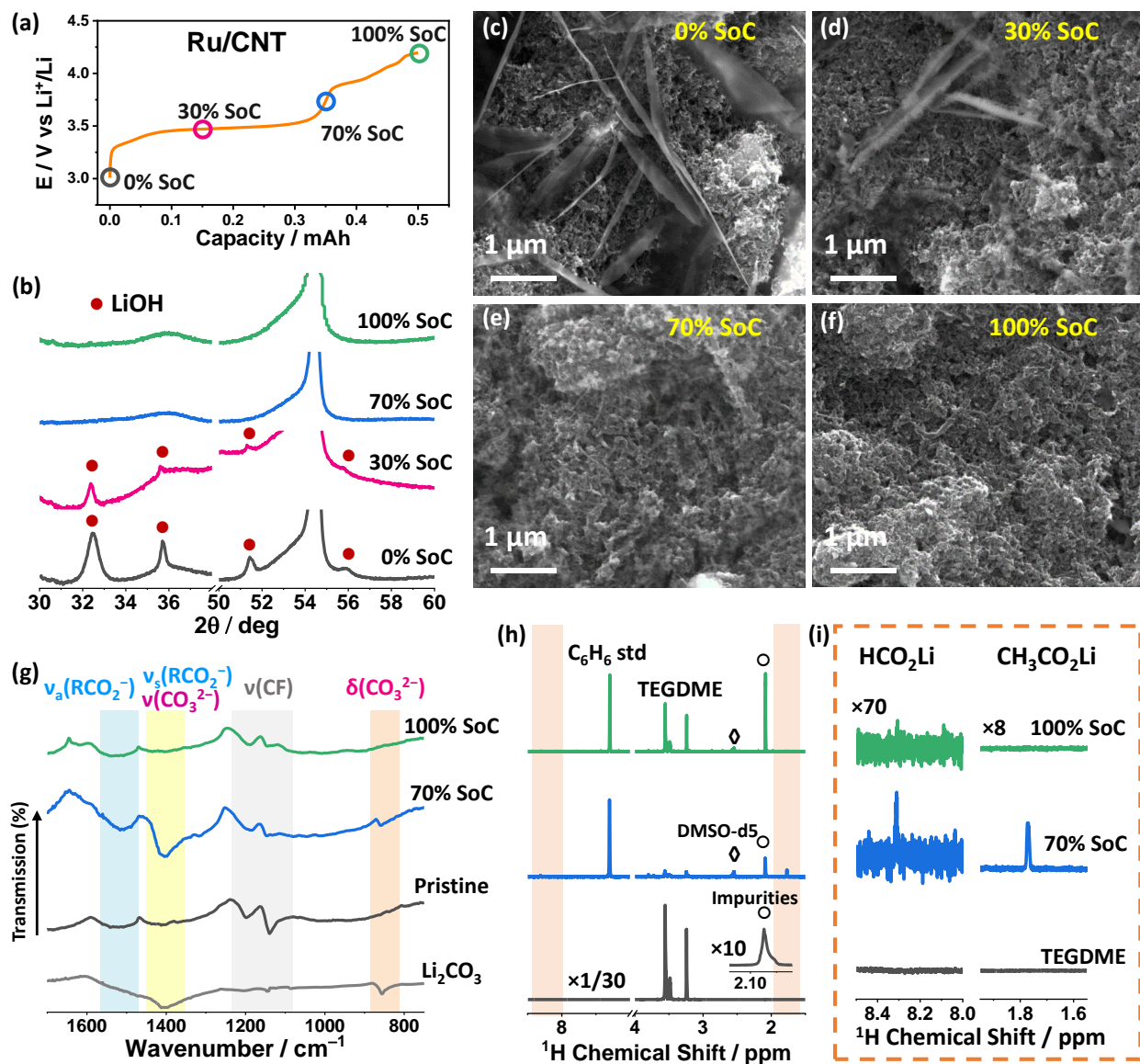
Figure 5 | The *ex-situ* characterization of charge products in TEGDME-based electrolytes at different state of charge. (**a**) The voltage profile of Ru/CNT cathode in 20%-H₂O/TEGDME electrolyte showing the various of state of charge (0%, 30%, 70%, and 100% SoC). (**b**) The XRD patterns of the Ru/CNT cathodes in 20%-H₂O/TEGDME electrolyte at the state of charge of 0% SoC, 30% SoC, 70% SoC, and 100% SoC, confirming that the first charge plateau is associate with the two-phase reaction mechanism. (**c–f**) The SEM images of the Ru/CNT cathodes in 20wt% H₂O electrolyte at the state of charge of (**c**) 0% SoC, (**d**) 30% SoC, (**e**) 70% SoC, and (**f**) 100%

SoC. (**g**) FTIR spectra of pre-loaded Li_2CO_3 electrode and various Ru/CNT cathodes (pristine, 70% SoC, and 100% SoC), showing that Li_2CO_3 and RCO_2Li forms at the end of first charge plateau. (**h, i**) ^{1}H NMR spectra and zoomed part of pure TEGDME and the extracts by D_2O from the cycled Ru/CNT cathodes at 70% SoC and 100% SoC, revealing that the side products (e.g., lithium formates and acetates) forms at 70% SoC but disappears at 100% SoC. We note that the TEGDME solvents (3–4 ppm) were still left on the cathode even after wash, the peak at 2.5 ppm is from internal standard DMSO-d5, and the peak at near 2.08 ppm (*) could be assigned to the impurities in the TEGDME or the trace acetonitrile vapor contaminated during the extraction process inside glove box.
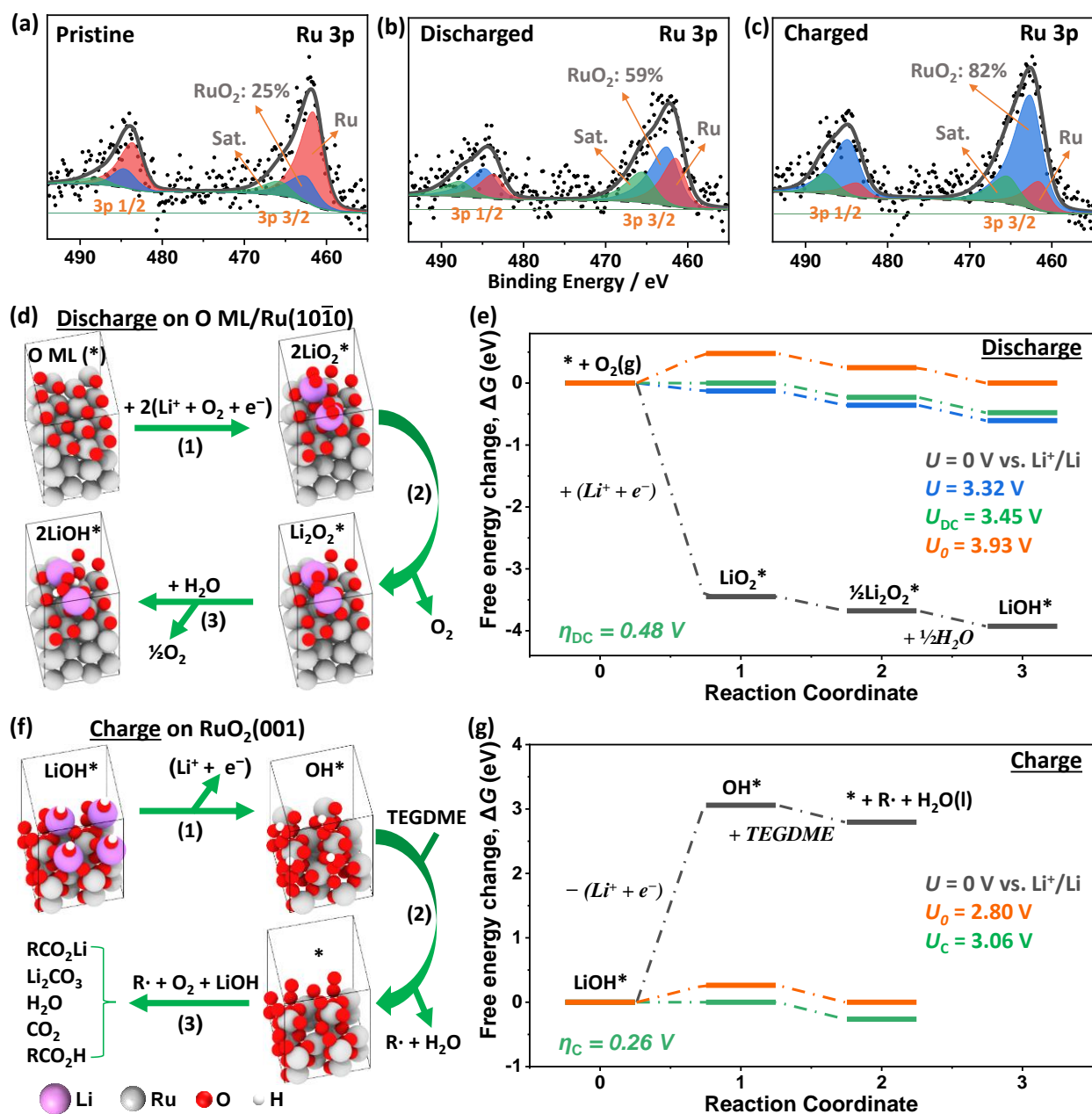
Figure 6 | Proposed reaction mechanisms of LiOH chemistry. (**a–c**) XPS Ru 3p spectra of Ru/CNT cathodes at (**a**) pristine, (**b**) discharged, and (**c**) charged states. (**d,f**) The proposed reaction pathways and structural models for LiOH chemistry with Ru/CNT catalyst in the presence of water: (**d**) discharge on O monolayer (ML)/Ru($10\bar{1}0$) surface and (**f**) charge on RuO_2(001) surface. The color of atoms in structure models: Li, purple; Ru, gray; O, red; H, white. (**e,g**) The corresponding energy diagrams using DFT calculations for (**e**) discharge and (**g**) charge reactions

at various potentials. The $\textbf{R}\cdot$ in $\textbf{f}$ and $\textbf{g}$ represents H-atom abstracted TEGDME$\cdot$ radical, which can decompose in O_2 to carboxylic acids (RCO_2H) and CO_2 that further react with LiOH to form lithium carboxylates (RCO_2Li) and Li_2CO_3. Besides, equilibrium potentials for discharge and charge in $\textbf{e}$ and $\textbf{g}$ can be easily calculated by $U_0 = -\Delta G^0/ne$, yielding $U_0 = 3.93$ V for discharge and $U_0 = 2.80$ V for charge.